

## Nested-Model Simulation of Moist Convection: The Impact of Coarse-Grid Parameterized Convection on Fine-Grid Resolved Convection

THOMAS T. WARNER

*National Center for Atmospheric Research,\* and  
Program in Atmospheric and Oceanic Sciences, University of Colorado, Boulder, Colorado*

HSIAO-MING HSU

*National Center for Atmospheric Research, Boulder, Colorado*

(Manuscript received 12 February 1999, in final form 3 September 1999)

### ABSTRACT

Future-generation, operational, weather prediction systems will likely include storm-scale, limited-area models that will explicitly resolve convective precipitation. However, the high-resolution convection-resolving grids will need to be embedded, or nested, within coarser-resolution grids that will provide lateral-boundary conditions. It is the purpose of this study to illustrate how the convective environment on a convection-resolving storm-scale model grid, and therefore the convection itself, can be significantly influenced by the treatment of convection on the coarser grids within which the fine grid is embedded.

It was confirmed that, as in the actual atmosphere, mass-field adjustments resulting from convection in one area (the outer grids, in this case) affect the convection in other areas (the inner, convection-resolving grid). That is, the errors in precipitation timing, precipitation intensity, and the vertical distribution of latent heating, associated with the treatment of convection on the outer grids, greatly affect the explicit convection on the inner grid. In this case, the different precipitation parameterizations on the outer two grids produce up to a factor of 3 difference in the 24-h amount of explicit rainfall simulated on the inner grid. Even when the parameterization is limited to only the outer grid, with explicit precipitation on both the middle and inner grids, over a factor of 2 difference in 24-h total explicit rainfall is produced on the inner grid. The different precipitation parameterizations on the outer grids appear to differently modulate the intensity and the timing of the explicit convection on the inner grid through induced subsidence.

### 1. Introduction

With improved methods of assimilating nonstandard data, such as from the Weather Surveillance Radar-1988 Doppler (WSR-88D), and with faster computing platforms, future-generation, very-limited-area operational weather prediction models will likely be used for explicit forecasting of convective storms. One example of this trend is that the National Oceanic and Atmospheric Administration's (NOAA) Forecast Systems Laboratory (FSL) is currently developing and testing prototype, operational, models with computational domains that have the area of one or two states (Schultz 1998; Szoke et al. 1998). Also, the University of Oklahoma's Center

for the Analysis and Prediction of Storms is running daily a convection resolving version of the Advanced Regional Prediction System model (Carpenter et al. 1998). An unavoidable situation with storm-scale models is that convection-resolving computational domains will need to be nested within, and obtain their lateral-boundary conditions (LBCs) from, coarser-resolution domains on which the convection must be parameterized. The problem to be addressed in this paper is the sensitivity of the explicitly resolved convection to physical inconsistencies in the parameterized convection.

Warner et al. (1997), in a review of LBC requirements for limited-area models, state the general rule that when two domains are nested, their convective parameterizations (CPs) should be the same, or similar, in order to minimize inconsistencies at the interface of the computational grids, whether the interface is two-way or one-way interacting. This is, in practice, a condition that is difficult to implement because specific CPs are often only valid over a limited range of scales, and the scales resolved on the different grids in a nested system differ. A potentially more serious problem may arise in the

---

\* The National Center for Atmospheric Research is sponsored by the National Science Foundation.

---

*Corresponding author address:* Thomas T. Warner, NCAR/RAP, P.O. Box 3000, Boulder, CO 80307-3000.  
E-mail: warner@ucar.edu

storm-scale model applications where one grid utilizes a CP and another nested within it explicitly resolves convection. This problem will be addressed in this study. Specifically, we will demonstrate the sensitivity of the explicit simulation of convection to the existence of, and the nature of, the CPs on the grids that provide lateral-boundary conditions for the convection-resolving grid. This is a very practical problem that must be addressed and understood in order for storm-scale operational prediction of convective weather to be successful.

Weisman et al. (1997) suggest, based on numerical simulations of a squall line, that models with grid increments as large as 4 km can explicitly reproduce much of the mesoscale structure and evolution obtainable from higher-resolution convection-resolving models with grid increments of, say, 1 km. Thus, because of computational constraints, it is likely that early-generation, operational, convection-resolving models applied in mid-latitudes will employ grid increments of from 2 to 4 km. Given the fact that grid nests generally involve resolution steps of three to four between grids, the next-coarser mesh within which the convection-resolving grid is embedded will have a grid increment of about 10 km. This raises the question regarding whether to utilize a CP on this grid, or to attempt to explicitly resolve the convection and employ a CP only on the even-coarser grids. Even though CP scale-separation assumptions are clearly highly questionable at this resolution [i.e.,  $\Delta x \sim 10$  km; Molinari and Dudek (1992)], Wang and Seaman (1997) have shown that the use of a CP and a grid increment of 12 km produces a superior quantitative precipitation forecast (QPF) than the use of the same CP and a grid increment of 36 km. Additionally, the National Weather Service's National Centers for Environmental Prediction (NCEP) have produced routine daily forecasts with a version of the Eta Model that has a grid increment of 10 km and that employs a CP (Black et al. 1998). Conversely, semioperational model forecasts have been performed by NOAA FSL without any CP, on grids with an 8-km grid increment (Snook et al. 1998), and the University of Oklahoma's Center for the Analysis and Prediction of Storms is running the Advanced Regional Prediction System model daily, in real-time mode, where the model has a 9-km grid increment and no parameterized precipitation (Carpenter et al. 1998). Even though the above simulations and forecasts of convection have shown promise, Cram et al. (1992) describe how a 5-km grid increment model was not able to explicitly simulate squall-line precipitation, and they attributed this failure to the fact that the excessively large grid increment did not permit the accurate explicit simulation of the convection. Seaman et al. (1998) also report difficulty in explicitly simulating a line of convection with a 4-km grid-increment domain, but the difficulty was related to poorly parameterized convection on the surrounding grid, which had a 12-km grid increment. Molinari and Dudek (1992)

provide an excellent critical review of the successes and failures associated with the use of CPs in mesoscale models. Clearly there is uncertainty in the modeling community regarding the relationship between model resolution and the need to parameterize convection.

The work described here addresses questions that are related to the needs and uncertainties described above.

- To what degree is the QPF associated with explicitly resolved convection on a model fine grid affected by the existence of parameterized convection on coarser grids within which the fine grid is embedded?
- How sensitive is the explicitly resolved convection on the inner grid to the specific choice of CP employed on outer grids?
- When nesting down from NWS Meso Eta Model resolutions ( $\Delta x \sim 30$  km) to resolutions that are potentially capable of explicitly resolving convection ( $\Delta x \sim 3$  km), what is the influence on the fine-grid QPF of the decision to parameterize, versus explicitly resolve, the convection on the intermediate-resolution grid ( $\Delta x \sim 10$  km)?
- How successful is the model employed here at simulating convection using a 3-km grid increment?

A case of summer season convection in the southwest United States is used as the basis for this study. The modeling system employed here is positioned over the complex terrain surrounding the White Sands Missile Range, New Mexico, and is a component of an operational forecasting system that is being developed by the National Center for Atmospheric Research (NCAR) for various U.S. Army Test and Evaluation Command (ATEC) test ranges (Davis et al. 1998). Because the terrain is complex, and the synoptic-scale forcing is weak in this case, the convection is diurnally forced and modulated by the orography. Because the simulation is not initialized with convective-scale data, it is reasonable that the locations of the convective activity will be deterministically predicted only to the extent that the convection is focused by the orography and other sources of differential heating that are related to the surface energy budget. Thus, the metrics used for quantitative validation of the simulations on the convection-resolving grid will be the total amount of precipitation on the grid, and its temporal distribution during the heating cycle. Qualitative comparisons will be made of the observed and simulated spatial distributions of the rainfall.

Section 2 will document the modeling system employed, provide a summary of the experiments, and describe the techniques used for validation of the simulations. In section 3 the meteorological case will be summarized, and in section 4 the results of the simulations will be described. A summary and discussion of the results will be provided in section 5.

## 2. Experimental design

### *a. Description of the model*

The model used in this study is the Pennsylvania State University-NCAR nonhydrostatic Mesoscale Model,

version 5. For details about this modeling system, refer to Dudhia (1989, 1993), Grell et al. (1994), Warner et al. (1992), and Davis et al. (1998). The planetary boundary layer parameterization, based on Troen and Mahrt (1986) and Hong and Pan (1996), is the MRF technique, which is employed in the Medium-Range Forecast Model of NCEP. For the precipitation parameterization, three approaches are employed: the Betts–Miller technique (Betts and Miller 1993; Janjic 1994), the Kain–Fritsch technique (Kain and Fritsch 1990, 1993), and the Grell technique (Grell 1993). These CPs are in common use by the mesoscale modeling community and have been well tested. A simple explicit treatment of cloud microphysics is employed and is based on Dudhia (1989). Both ice and liquid phases are permitted for cloud and precipitation, but mixed phases are not permitted. The model uses a radiation scheme in which longwave and shortwave radiation interact with the clear atmosphere, cloud, precipitation, and the ground (Dudhia 1989).

The triply nested computational grids are depicted in Fig. 1a. The inner (grid 3), middle (grid 2), and outer (grid 1) computational grids have mesh sizes of  $61 \times 61$ ,  $67 \times 70$ , and  $84 \times 98$  points and grid increments of 3.3 km, 10 km, and 30 km, respectively. The nested grids, each with 35 computational layers, interact during the simulation (i.e., information is passed across the interface in both directions, and each finer-grid solution replaces the coarser-grid solution in the coincident area at the end of its calculations). Figure 1 also shows the topography for the middle grid (Fig. 1b) and the inner grid (Fig. 1c). On the inner grid, the north–south-oriented Rio Grande Valley is on the west side, with the San Andres Mountains, the Tularosa Valley, and the Sacramento Mountains to the east. The vertical distribution of the computational layers is shown in Fig. 2. The model top is located at 50 hPa.

The horizontal extent and the number of levels of the computational grids are dictated by constraints associated with the fact that this model must run operationally. Specifically, a 24-h forecast must be available within a couple of hours, with the model calculations being performed on an eight-processor, Silicon Graphics Origin 2000. Because the problem being addressed in this study is related to the operational prediction of convection, it is appropriate that the model configuration used be realistic in terms of adhering to current operational constraints. It is recognized that higher horizontal resolution on the finest grid would have been better able to define smaller-scale convective processes. However, even though not ideal, the 3.3-km grid increment should be adequate and represents the best that could be utilized in the operational system.

The model initial conditions are defined through the use of radiosonde and surface data, where the first-guess field is the NCEP global,  $2.5^\circ \times 2.5^\circ$  analysis. Lateral-boundary conditions for the outer grid, grid 1, are defined using linear temporal interpolations between 12-hourly NCEP global analyses.

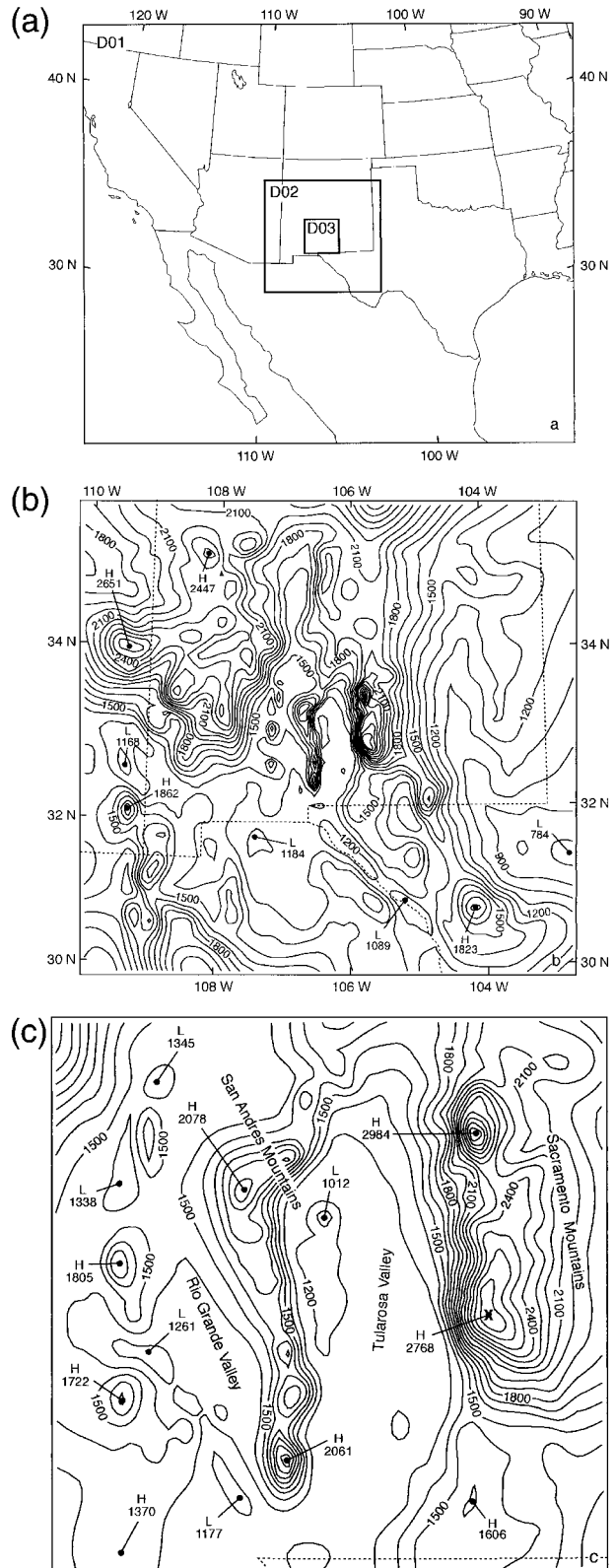


FIG. 1. Area coverage for computational domains (grids) (a) 1, 2, and 3; topography for (b) grids 2 and (c) 3. The contour interval is 100 m.

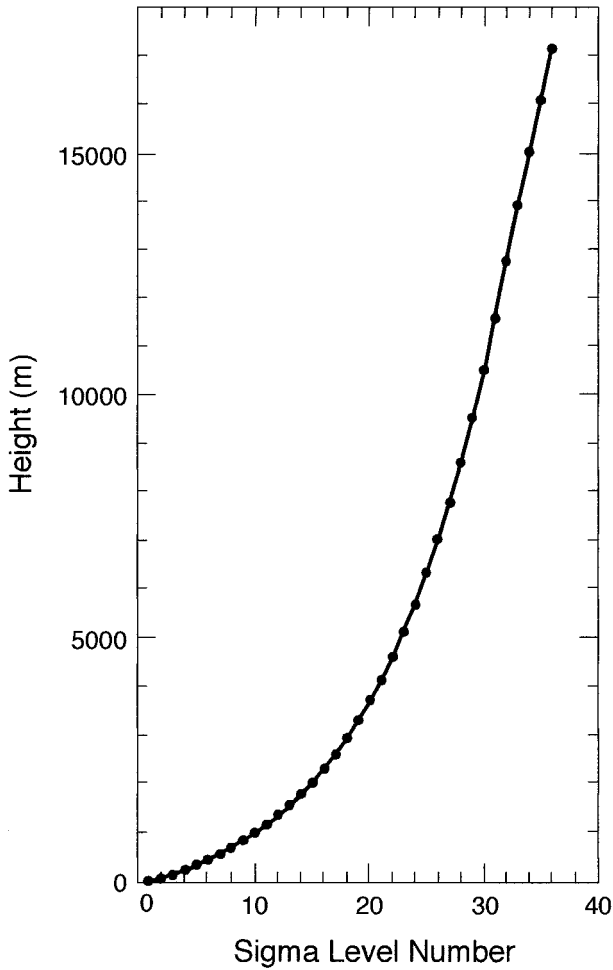


FIG. 2. Vertical distribution of the computational layers in the model. The dots represent the interfaces between the 35 layers.

*b. Summary of experiments*

The experiments are summarized in Table 1. There are two main series of experiments. In one series (G12E3, BM12E3, KF12E3), the outer two grids of the triply nested modeling system employ a CP, where the inner grid has only resolved precipitation. The three CPs, noted in section 2a above, are tested, where the same CP is used on both outer grids. The second series of experiments (G1E23, BM1E23, KF1E23) is identical, except that the CP is used only on the outer grid, with no CP employed on the inner two grids.

In order to diagnose the effects of outer-grid CPs on the temperature and moisture fields that define the convective environment of the inner grid, four experiments are employed. In all four experiments, no precipitation processes are permitted on grid 3 because the objective is to isolate the direct effects of the outer grid CPs on the grid 3 environment. In three of the experiments, each of the CPs is used on both grids 1 and 2 (G12D3, BM12D3, KF12D3). In the fourth experiment, no precipitation processes are permitted on any of the grids (D123). Comparison of the grid 3 convective environment from any one of the first three experiments with that from the fourth isolates the effects on that environment of the outer grid CP.

Three additional experiments involved various approaches for eliminating the use of outer-grid CPs. In one (E123), only explicit convection was permitted on all three computational grids. In a second, all precipitation effects were eliminated from the outer two grids (D12E3). In a third (E3), the two outer grids were eliminated, and the lateral-boundary conditions of the convection-resolving grid were defined based on the NCEP large-scale analysis.

It is important to be reminded of the fact that the objective of the use of a nested operational modeling system, such as this one, is to produce an accurate fore-

TABLE 1. Summary of experiments. The abbreviations in the experiment designations are as follows: G refers to the Grell CP, KF refers to the Kain-Fritsch CP, BM refers to the Betts-Miller CP, E refers to the explicit representation of convection, D refers to “dry” physics with no moist processes, 1 refers to the grid with  $\Delta x = 30$  km, 2 refers to the grid with  $\Delta x = 10$  km, and 3 refers to the grid with  $\Delta x = 3.3$  km. For example, in experiment G12E3, the Grell parameterization is used on grids 1 and 2, and the explicit representation for convection exists on grid 3.

Experiment	Convection representation		
	30 km $\Delta x$ grid	10 km $\Delta x$ grid	3.3 km $\Delta x$ grid
G12E3	Grell	Grell	Explicit
BM12E3	Betts-Miller	Betts-Miller	Explicit
KF12E3	Kain-Fritsch	Kain-Fritsch	Explicit
G1E23	Grell	Explicit	Explicit
BM1E23	Betts-Miller	Explicit	Explicit
KF1E23	Kain-Fritsch	Explicit	Explicit
G12D3	Grell	Grell	None-dry
BM12D3	Betts-Miller	Betts-Miller	None-dry
KF12D3	Kain-Fritsch	Kain-Fritsch	None-dry
D123	None-dry	None-dry	None-dry
E123	Explicit	Explicit	Explicit
E3	No grid	No grid	Explicit
D12E3	None-dry	None-dry	Explicit

cast on the inner grid. The middle and outer grids exist simply to provide reasonable boundary conditions for the inner grid. Thus, the various experiments represent different approaches for treating convection on the outer grids, where the goal is to provide reasonable larger-scale convective-environment information to the fine grid.

The simulations were 24 h in duration, from 1200 UTC (0500 LST) 12 August to 1200 UTC 13 August 1997. The simulation length is dictated by ATEC test range operational requirements and our desire to assess forecast skill for at least one diurnal cycle.

### c. Verification techniques

Because of the paucity of rain gauge data on the convective scale, especially in this geographic area, the 1.5-km above sea level (ASL) reflectivity from the WSR-88D radar at Holloman Air Force Base was translated to rain rate for the innermost model grid using the standard Marshall–Palmer relationship,  $Z = 200R^{1.6}$ , where  $Z$  is reflectivity and  $R$  is rain rate. This 1.5 km ASL reflectivity analysis was obtained by interpolation from low-level radar scans. These radar-inferred rain rates compare favorably with gauge data in the Tularosa Valley. Because the objective of this study is to determine the sensitivity of the rainfall simulation on this inner convection-resolving grid (grid 3) to the coarse-grid parameterized convection, it is these rainfall fields that will serve as the main focus of the verification.

The rainfall simulations on grid 2, the middle (10 km) grid, are evaluated to determine whether it is more skillful to resolve or to parameterize convection at that resolution. Also, rainfall simulation errors on the 10-km grid influence errors in the rainfall simulation on the inner grid. For verification outside the area of the innermost grid, where the Holloman radar does not provide coverage, the NCEP multisensor National Precipitation Analysis and gauge data are employed. The NCEP analysis is produced through a combination of gauge data and gauge-corrected WSR-88D precipitation estimates. Unfortunately, even though the NCEP analysis does capture the main area of rainfall in this case, in eastern New Mexico and the western Texas panhandle, it is suspect over the western part of grid 2 where no rainfall is analyzed even though gauge data and Next-Generation Weather Radar (NEXRAD) National Mosaic Reflectivity Images (available from the NOAA National Climatic Data Center) imply the existence of some scattered rain accumulation.

The simulated and radar-inferred temporal distributions of grid-total hourly rainfall on grids 2 and 3 are quantitatively compared in terms of 1) the amount of precipitation and 2) the temporal distribution of the precipitation during the heating cycle. In addition, radar-inferred and simulated spatial distributions of 24-h total accumulations will be qualitatively compared.

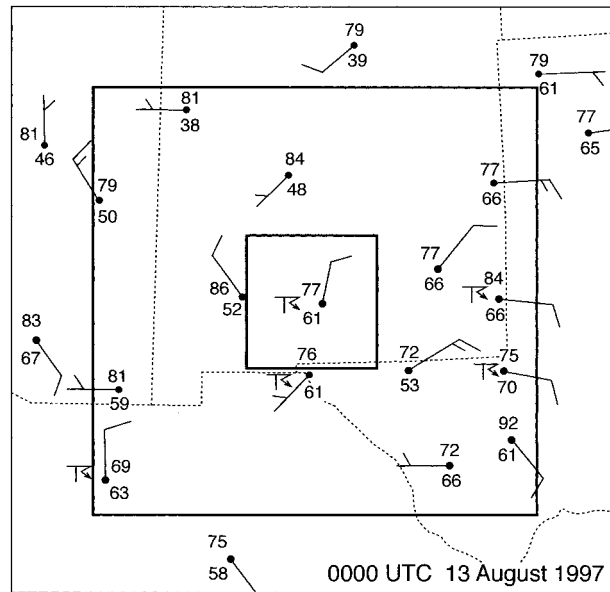


FIG. 3. Regional surface analysis for 0000 UTC 13 Aug 1997 showing wind, temperature (F), and dewpoint temperature (F) for an area that is slightly larger than grid 2. A long line on the wind staff represents 10 kt and a short line represents 5 kt. For each station, the upper number is temperature and the lower number is dewpoint temperature.

### 3. Description of the meteorological conditions

During the 24-h period of this study, from 1200 UTC 12 August to 1200 UTC 13 August 1997, a weak low pressure system moved from northern Missouri to northern New York State. The cold front extending southwest from this low ended in New Mexico as a weak stationary front, which drifted southward from the middle to the southern part of the state during the period. Figure 3 shows the regional surface wind conditions at 0000 UTC 13 August. Speeds are in the range of 5–10 kt ( $2.6\text{--}5.2\text{ m s}^{-1}$ ). At 700 hPa, the winds over New Mexico during the period are generally from the west or southwest at  $10\text{--}15\text{ m s}^{-1}$  (not shown). The 500-hPa conditions for 1200 UTC 12 August, shown in Fig. 4, are also quite barotropic. Figure 5 shows the early morning El Paso temperature and dewpoint temperature profiles for 1200 UTC 12 August. The lower troposphere below 700 hPa exhibits dewpoint depressions of  $5^{\circ}\text{--}10^{\circ}\text{C}$ , and there is a hint of a humid layer at 650 hPa. The observed weak vertical shear is consistent with fact that the atmosphere supported disorganized multicellular convection rather than more organized convection on this day. Typical convective available potential energy (CAPE) under such conditions ranges from 300 to  $1000\text{ J kg}^{-1}$ .

Figure 6 shows the grid 3, 24-h rainfall based on the Holloman radar. Precipitation was observed over the higher elevations of the Sacramento Mountains; in the Tularosa Valley, with greater accumulations in the south; over the New Mexico border with Texas; and (scattered) over the Rio Grande Valley of New Mexico. Even

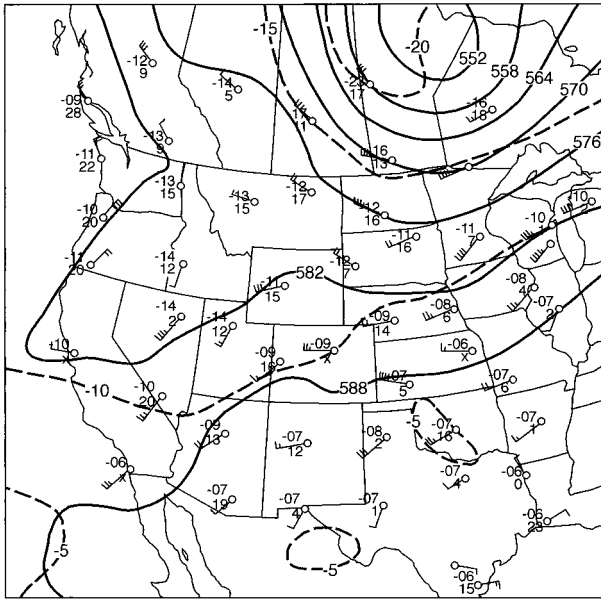


FIG. 4. Winds, temperatures, dewpoint depressions, and heights at 500 hPa for 1200 UTC 12 Aug 1997. The temperatures (dewpoint depression) in  $^{\circ}\text{C}$  are shown in the upper (lower) left of the station location. Long (short) barbs on the wind staff represent 10 (5)  $\text{m s}^{-1}$ . The solid lines are heights in decameters plotted at an interval of 60 m, and the dashed lines are temperature in  $^{\circ}\text{C}$  plotted at an interval of  $5^{\circ}\text{C}$ .

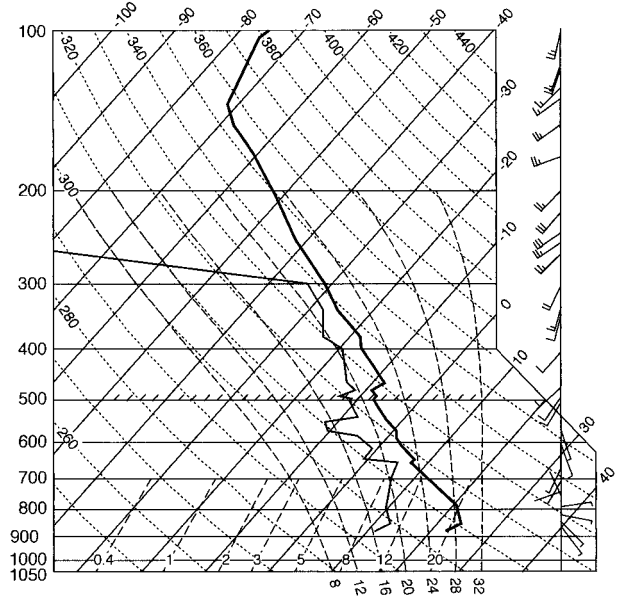


FIG. 5. El Paso, TX, temperature and dewpoint temperature profiles for 1200 UTC 12 Aug 1997.

though the 1.5-km elevation reflectivity data used for this figure do not show rainfall to the east of the Sacramento Mountains, significant reflectivity is observed there in data from higher-elevation scans. Figure 7 displays the 24-h rainfall for both grids 2 and 3, based on the NCEP multisensor precipitation analysis, the Holloman WSR-88D radar, and gauge data. The SE symbols denote areas where the NEXRAD National Mosaic Reflectivity Images (not shown) show scattered echoes of 35–55 dBZ at various times during the day.

**4. Results of the experiments**

*a. Analysis of grid-total hourly precipitation*

In the first series of three experiments, the same CPs were used on both of the outer two grids. The aforementioned three CPs were employed: the Kain–Fritsch, Betts–Miller, and Grell techniques. Figure 8 shows the grid-3-average simulated hourly precipitation rate for these three experiments (KF12E3, BM12E3, G12E3), and the grid-3-average observed hourly precipitation rate, as inferred from the Holloman WSR-88D. Also shown is the simulated hourly precipitation from the experiment that used no CP on any of the grids (E123). It is worth being reminded that these plots are for grid 3 only, where the model physics on this grid are identical for all experiments. All differences result from the different effects of the convection on grids 1 and 2 being

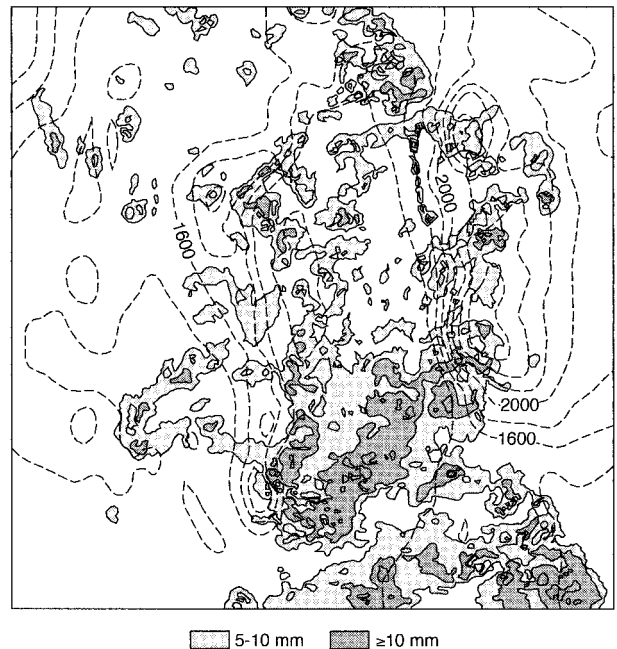


FIG. 6. Total observed rainfall for the 24-h period from 1200 UTC 12 Aug to 1200 UTC 13 Aug 1997 for grid 3, based on radar reflectivity from the WSR-88D at Holloman, NM. Isohyets are plotted at irregular intervals with the following values (mm): 5, 10, 20, 30, and 40. Light shading reflects amounts of 5–10 mm, while darker shading is for values greater than 10 mm. The dashed lines show terrain elevation.

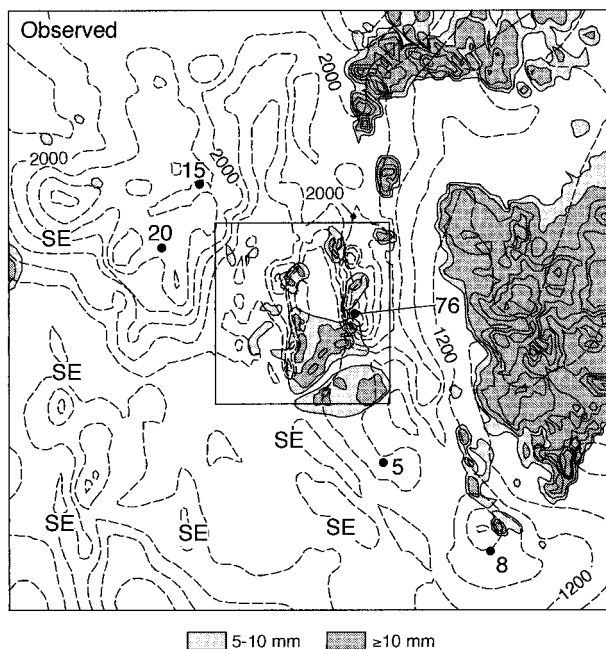


FIG. 7. Total observed rainfall for the 24-h period from 1200 UTC 12 Aug to 1200 UTC 13 Aug 1997 for grids 2 and 3. The analysis for the area covered by grid 3 is identical to the Holloman-radar-based analysis in Fig. 4. The analysis outside of that area is based on the NCEP multisensor precipitation analysis. Isohyets are plotted at irregular intervals with the following values (mm): 5, 10, 20, 30, and 40. Light shading reflects amounts of 5–10 mm, while darker shading is for values greater than 10 mm. Numbers show rain gauge measurements (mm) in areas where no echoes are reported in the NCEP or Holloman radar analyses. The SE symbols indicate general areas where scattered echoes of intensity 35–55 dBZ are reported during the period in the NEXRAD National Mosaic Reflectivity Images available from the NOAA National Climatic Data Center.

passed through the nest interface to grid 3, and there affecting the explicit precipitation.

The plot of radar-inferred precipitation clearly shows a diurnal cycle to the convection, with a peak rain rate at about 1500 LST. There is significantly more total precipitation volume after the time of this maximum than before. For all three CPs employed on grids 1 and 2, the grid-3-simulated rainfall has the following characteristics: 1) significant rainfall correctly begins at about 1000 LST and increases at the correct rate for the next 2–3 h, 2) there is a diurnal cycle to the precipitation, and 3) the amounts are generally underpredicted. With the Grell and Betts–Miller CPs on grids 1 and 2, there is a bimodal distribution to the rainfall on grid 3, with maxima in both the afternoon and evening (as with the observed precipitation). Except for the Kain–Fritsch experiment, the time of the precipitation decay is simulated well. The simulation with no CP (E123) produces a rainfall rate maximum that is close to that observed, but G12E3 also reproduces well the overall observed temporal distribution. In general, the treatments of convection outside of grid 3 clearly have a considerable impact on the resolved precipitation on grid 3.

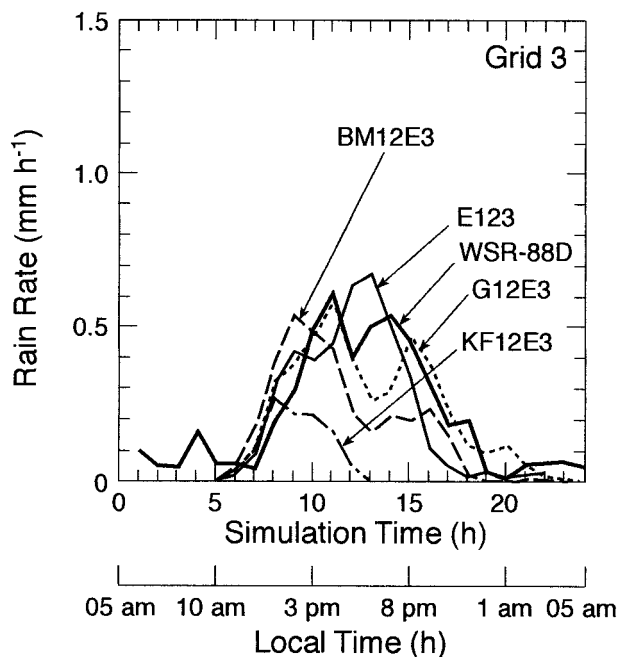


FIG. 8. Grid-3-average rain rate ( $\text{mm h}^{-1}$ ) as a function of time during the 24-h simulation from 1200 UTC (0500 LST) 12 Aug to 1200 UTC 13 Aug 1997. Plots are shown for experiments KF12E3, BM12E3, G12E3, and E123, and for the observed precipitation as estimated from the Holoman WSR-88D radar.

As a first step in understanding the mechanisms by which the grid 1 and 2 CPs influence the rainfall on grid 3, the grid-average hourly rain rates for grid 2 (excluding the area of grid 3) are plotted in Fig. 9 for each CP. As in Fig. 8, also plotted are the hourly rain rates from the experiment that used no CP on any of the grids, and the estimated observed average rain rate. As noted earlier, outside of grid 3 the observed rainfall estimate is based on the NCEP multisensor National Precipitation Analysis, which does not capture the scattered rainfall that existed over western New Mexico, west Texas, and northern Mexico. However, the bulk of the rain volume on this grid is associated with the large convective system over eastern New Mexico and west Texas, which is represented in the NCEP analysis. Thus the WSR-88D rainfall plot in Fig. 9 represents probably only a modest underestimate of the true amounts. The time of initiation of significant *observed* rainfall is ~2 h later than for grid 3, and the highest rates occur between 1700 and 2200 LST. Both the Kain–Fritsch and the Betts–Miller CPs trigger much too early. The Grell CP triggers at about the correct time, and the rainfall rates are realistic. Experiment E123 also initiates precipitation at about the correct time, but the maximum is a few hours late.

In the second series of experiments, consisting of experiments G1E23, KF1E23, and BM1E23, the use of CPs is limited to grid 1. Figure 10 shows that the overall timing of the explicit precipitation on grid 2 from ex-

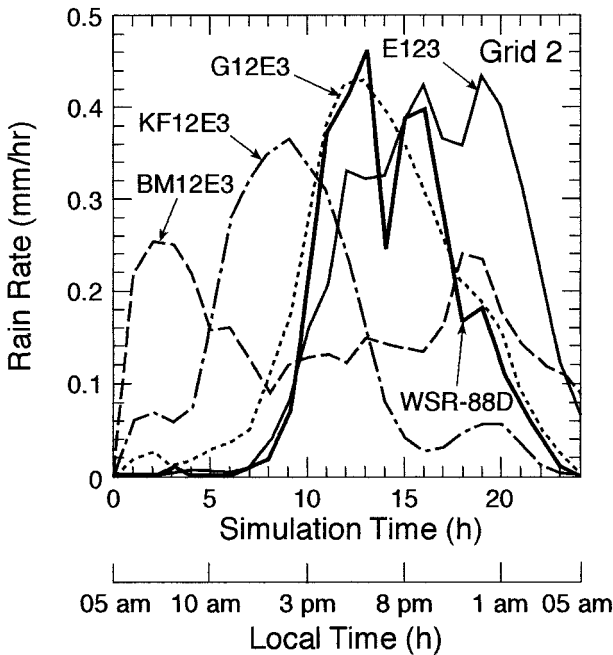


FIG. 9. Grid-2-average rain rate ( $\text{mm h}^{-1}$ ), excluding the area of grid 3, as a function of time during the 24-h simulations from 1200 UTC (0500 LST) 12 Aug to 1200 UTC 13 Aug 1997. Plots are shown for experiments KF12E3, BM12E3, G12E3, and E123, and for the observed precipitation as estimated by the NCEP multisensor precipitation analysis.

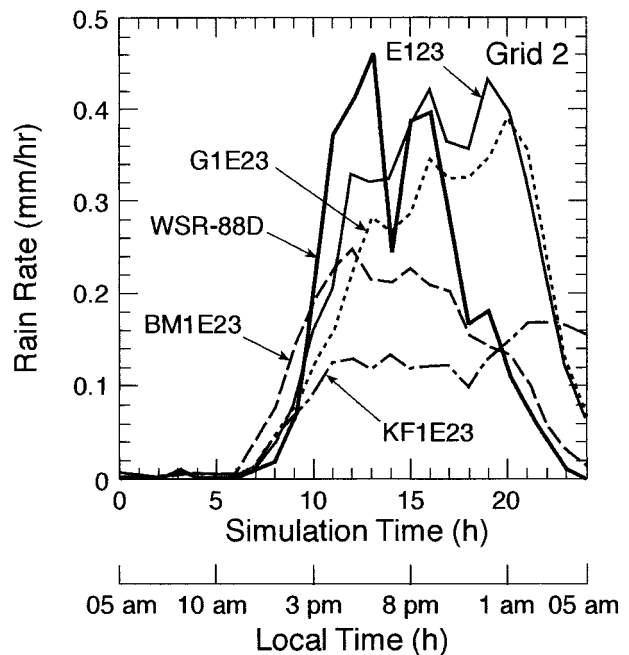


FIG. 10. Grid-2-average rain rate ( $\text{mm h}^{-1}$ ), excluding the area of grid 3, as a function of time during the 24-h simulations from 1200 UTC (0500 LST) 12 Aug to 1200 UTC 13 Aug 1997. Plots are shown for experiments KF1E23, BM1E23, G1E23, and E123, and for the observed precipitation as estimated by the NCEP multisensor precipitation analysis.

periments BM1E23 and KF1E23 is much better than that of the parameterized precipitation on the same grid in the previously described series (Fig. 9). However, the timing of the grid 2 precipitation maximum from the parameterization in G12E3 is better than that of the explicit precipitation in G1E23. The differences in the grid 2 rainfall among the experiments demonstrate its sensitivity to the grid 1 CP, analogous to the sensitivity of grid 3 explicit rainfall to the grid 1 and 2 CPs in the other series of experiments. Because the explicit rainfall on grid 2 does not occur prematurely in this series, as it does in the previous series for two of the CPs, this may allow for improved precipitation rates on grid 3. Figure 11, displaying the grid-average rainfall rates for grid 3 for these experiments, shows that the grid 3 rainfall is sensitive to whether or not a CP is employed on grid 2 (i.e., compare analogous curves in Figs. 8 and 11). With the use of the Kain–Fritsch and Betts–Miller schemes limited to grid 1, about twice as much rainfall is produced on grid 3. With the use of the Grell scheme limited to grid 1, some differences are apparent, but the impact is not great.

The differences shown in Fig. 11 in the grid 3 rainfall associated with the use of the three different CPs, and with no CP, on grid 1 are surprising, given that the physics are the same on both grids 2 and 3. The four, grid 3 solutions begin to diverge at about hour 8, or 1300 LST. It is at about this time that the grid 2 explicit rainfall begins to be affected by the different grid 1 CPs,

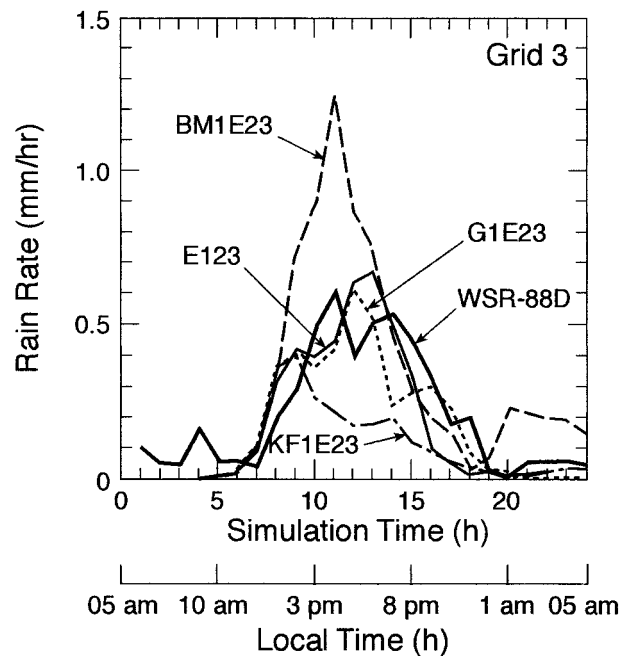


FIG. 11. Grid-3-average rain rate ( $\text{mm h}^{-1}$ ) as a function of time during the 24-h simulation from 1200 UTC (0500 LST) 12 Aug to 1200 UTC 13 Aug 1997. Plots are shown for experiments KF1E23, BM1E23, G1E23, and E123, and for the observed precipitation as estimated from the Holoman WSR-88D radar.

as seen in Fig. 10. Because the explicit convection on both grids 2 and 3 seems to be affected almost simultaneously, it would seem that mass-field adjustments that are initiated on grid 1 are responsible.

*b. Analysis of the spatial distribution of precipitation*

The analysis of the spatial distribution of the observed and simulated precipitation will be limited to the 24-h totals. Figure 12 shows the grid 3, 24-h rainfall for the seven simulations discussed thus far and should be compared with the Holloman-radar-based analysis in Fig. 6. Regarding Fig. 6, recall that beam blockage of the Holloman radar probably is responsible for underestimation of the rainfall to the east of the Sacramento Mountains. The model simulations all agree with the observations in terms of placing rainfall over the Sacramento Mountains. Of the three simulations with a CP on grid 2, G12E3 is best in terms of locating precipitation over the Tularosa Valley and over the Texas–New Mexico border in the southeastern corner of grid 3. All three produce scattered precipitation over the Rio Grande Valley. The four experiments with no CP on grid 2 all produce similar spatial distributions, except BM1E23 clearly has too much rainfall along the southern boundary of grid 3. None reproduce the observed rainfall in the central Tularosa Valley, as seen in G12E3.

Figure 13 displays the simulated 24-h rainfall for both grids 2 and 3 for experiments E123, KF1E23, and KF12E3, and should be compared with the analysis in Fig. 7. All three experiments correctly simulate rainfall to the east of the Sacramento Mountains, but the intensities and distributions vary. None simulate the extent of the observed rainfall over eastern New Mexico in the eastern part of grid 2 (Fig. 7). Experiment KF12E3 performs the best in this regard, but the rainfall is too far north and not sufficiently extensive. The use of explicit rainfall only, with no CP, on grid 2 (E123, KF1E23) produces excessive rainfall in the southwest quadrant of the grid over Mexico and southwestern New Mexico. In contrast, the Kain–Fritsch CP in KF12E3 seems to best replicate the scattered nature of the convection over much of grid 2 that is inferred by the NEXRAD National Mosaic Reflectivity Images (not shown) and the isolated but significant rain gauge amounts (Fig. 7). The coincidence of the rainfall boundary with the southern grid 2–3 interface in KF12E3 is obviously related to an inconsistency between the physics of the resolved and parameterized rainfall. Grid 2 rainfall patterns from the other four experiments (not shown—BM12E3, BM1E23, G12E3, G1E23) are qualitatively similar to those from E123 and KF1E23 (Fig. 13) in terms of underestimating the heavy rain in eastern New Mexico and overestimating it in the southwest quadrant of the domain over Mexico.

*c. Discussion of interactions among the grids that affect the fine-grid QPF*

Erroneous precipitation-related processes on grids 1 and 2 could contribute to precipitation errors on grid 3 through a number of hypothetical mechanisms. If the precipitation on grid 2 is immediately upstream of grid 3, errors could influence the tropospheric moisture and cause the air advecting onto grid 3 to be too moist or too dry to support the correct precipitation rates there. However, for this case the main area of grid 2 rainfall is to the east and downstream of grid 3. Alternatively, if a grid 2 CP is capable of producing outflow boundaries (e.g., the Kain–Fritsch CP), these could propagate through the grid interface and initiate convection. In fact, none were observed near the grid 2–3 interface in any of the simulations. Furthermore, given the physical distances between grid 3 and the grid 1 CP effects in the second series of experiments where no CP is used on grid 2, it is not likely that outflow boundaries or advection could be contributors to the observed grid 1 to grid 3 teleconnections over such large distances.

Another mechanism is related to the fact that the thermodynamic effects of the parameterized convection on grids 1 and 2 will be felt by grid 3 on gravity wave timescales through the modification of the grid 3 convective environment by the induced vertical motion. Differences in the grid 3 response to the different grid 1 CPs can be related to both the spatial and temporal distribution of the grid 1 parameterized convection, as well as to differences in the vertical distribution of the parameterized latent heating. Because of the aforementioned observed short timescale associated with the response of grid 3 convection to grids 1 and 2 convection for this case, it is hypothesized that physical inconsistencies in the parameterized convection on outer grids influence the timing and amplitude of the explicit convection on the inner grids through mass-field adjustments associated with the outer grids' latent heating. That is, differences in the amplitudes and vertical, horizontal, and temporal distributions of the latent heating among the CPs on outer grids produce different mass-field adjustments on the outer grids. The resulting gravity waves then propagate through the grid-nest interfaces to the inner convection-resolving grid in the system. Hence, the gravity wave response to the specific characteristics of CP latent heating determines the spatial and temporal distribution of the induced vertical motion on the fine grid. A simple example would be a case in which latent heating from parameterized convection is excessive on an outer grid, thus possibly producing excessive subsidence on the inner convection-resolving grid. Associated excessive drying and/or stabilization of lapse rates could erroneously inhibit the resolved convection. It is also probable that inappropriate vertical distributions of CP latent heat release could significantly and erroneously affect the characteristics of the induced vertical velocity on inner grids.

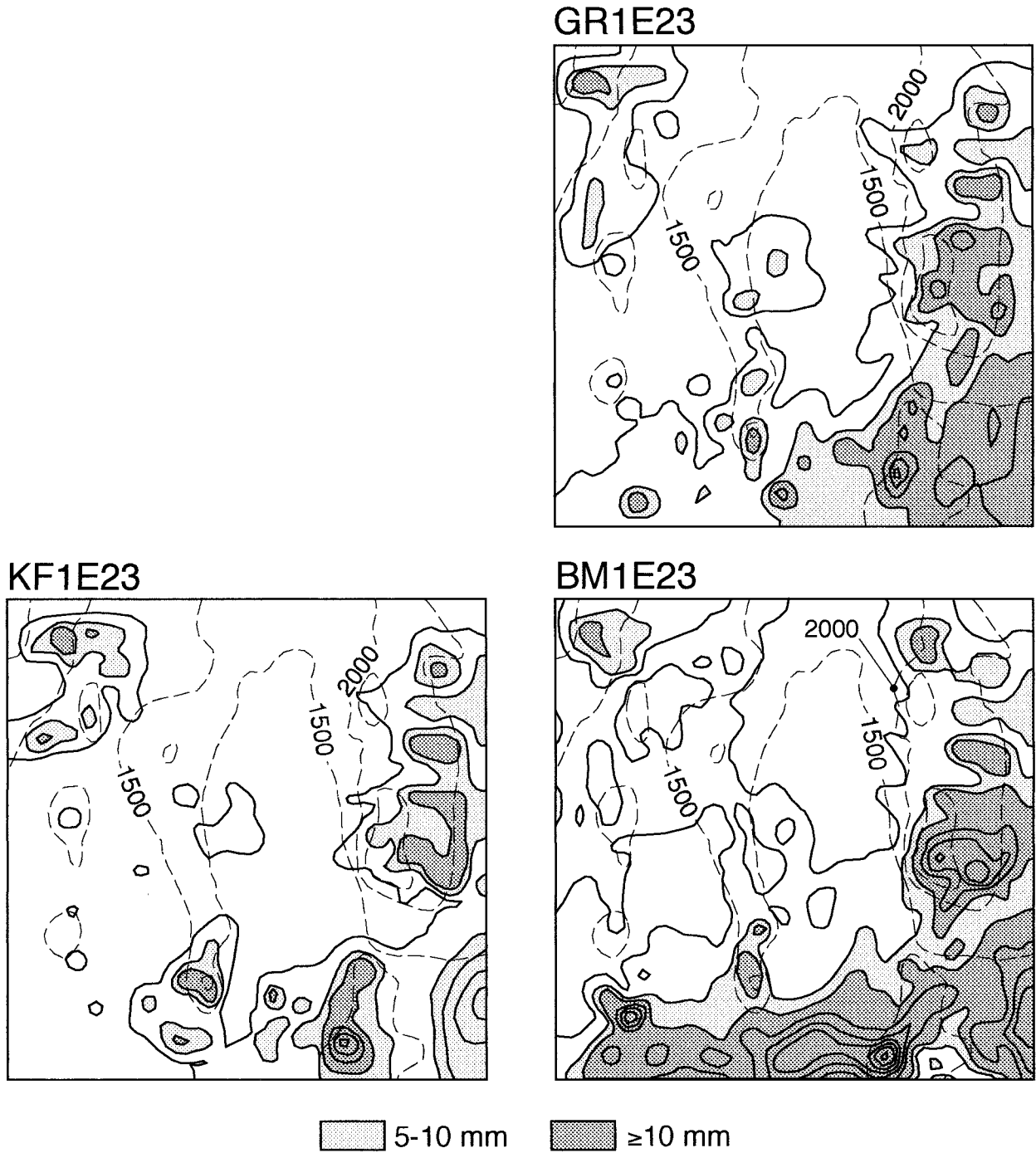
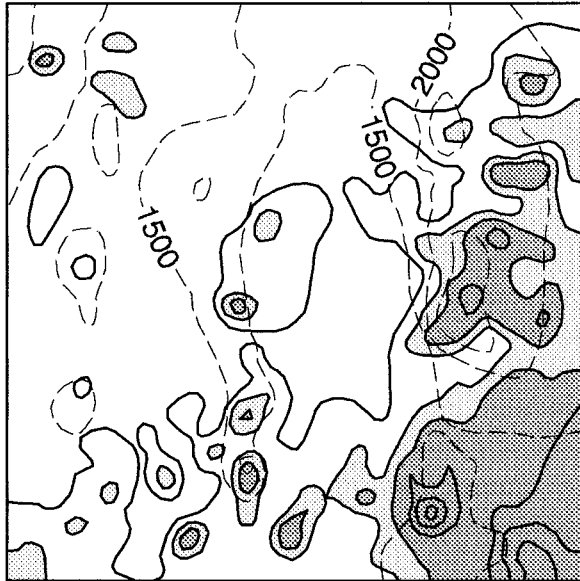


FIG. 12. Total simulated rainfall for the 24-h period from 1200 UTC 12 Aug to 1200 UTC 13 Aug 1997 for grid 3 for the designated seven experiments. Isohyets are plotted at irregular intervals with the following values (mm): 5, 10, 20, 30, and 40. Light shading reflects

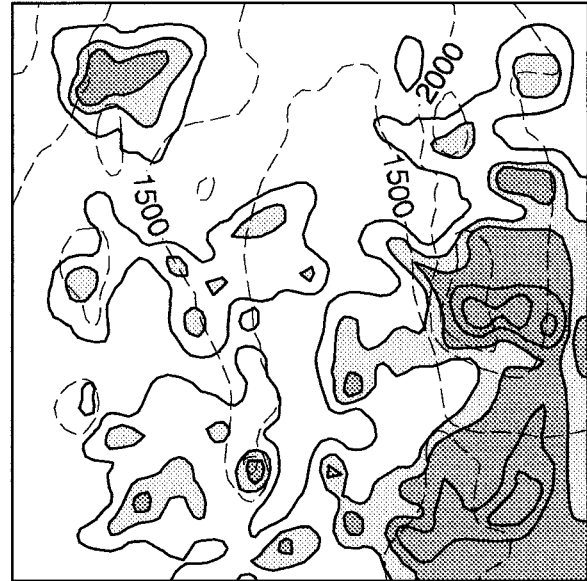
Before discussion of model simulation diagnostics that are aimed at quantifying the effects of outer grid CPs on the convective environment of inner, convection-resolving grids, a brief review will be provided of other work that describes the nature of the vertical motion field that surrounds areas of convective heating. Mapes (1993), Bretherton (1987), Pandya and Durran (1996),

Bretherton and Smolarkiewicz (1989), and Nicholls et al. (1991) provide good physical descriptions of the process. Specifically, compensating subsidence surrounding heated regions in the atmosphere is associated with propagating gravity wave pulses, which Mapes refers to as “buoyancy bores” because they are not ordinary periodic waves. Rotation and turbulent dissipation ef-

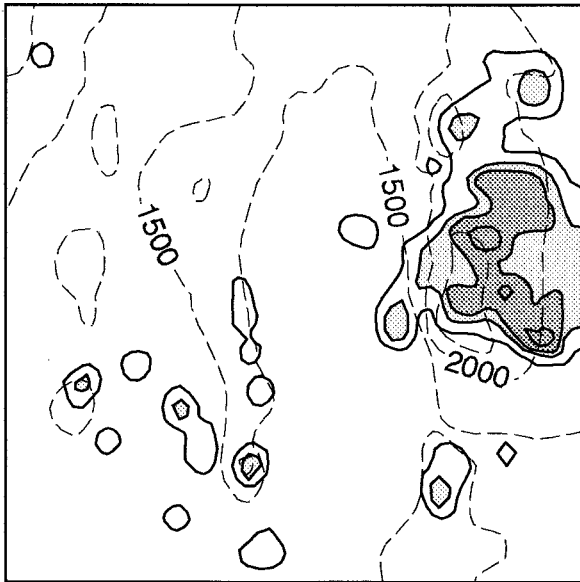
E123



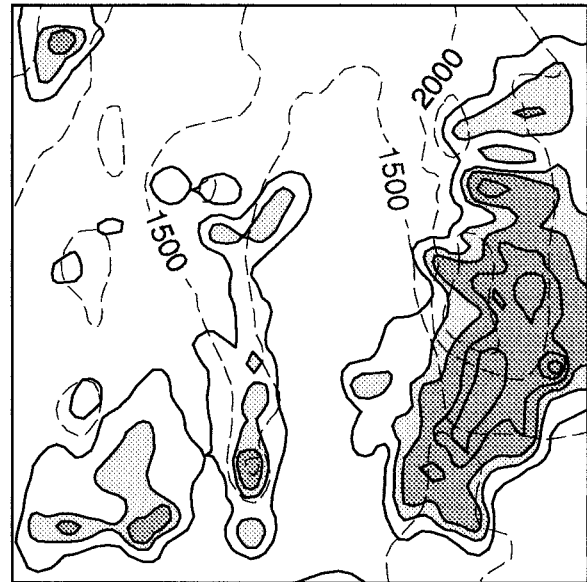
GR12E3



KF12E3



BM12E3



5-10 mm
   $\geq 10$  mm

FIG. 12. (Continued) amounts of 5–10 mm, while darker shading is for values greater than 10 mm.

fects impose a distance scale to the radial gravity wave propagation away from the region of heating, and therefore this radial distance scale applies to the vertical velocity response as well. The deeper modes, stimulated by deep latent heating, travel the fastest, and therefore propagate the farthest before absorption by rotation or dissipation effects. Thus, deeper modes dominate the atmospheric response at large distances, while shallow

modes are trapped nearer the heated region. Mapes (1993) and Nicholls et al. (1991) illustrate the vertical motion response to a positive-only heat source that excites two vertical modes: a deep one with a vertical wavelength that is twice the depth of the heating, and a shallower one with a wavelength that is equal to the depth of the heating. The deeper and faster mode generates a subsidence response over the depth of the heat-

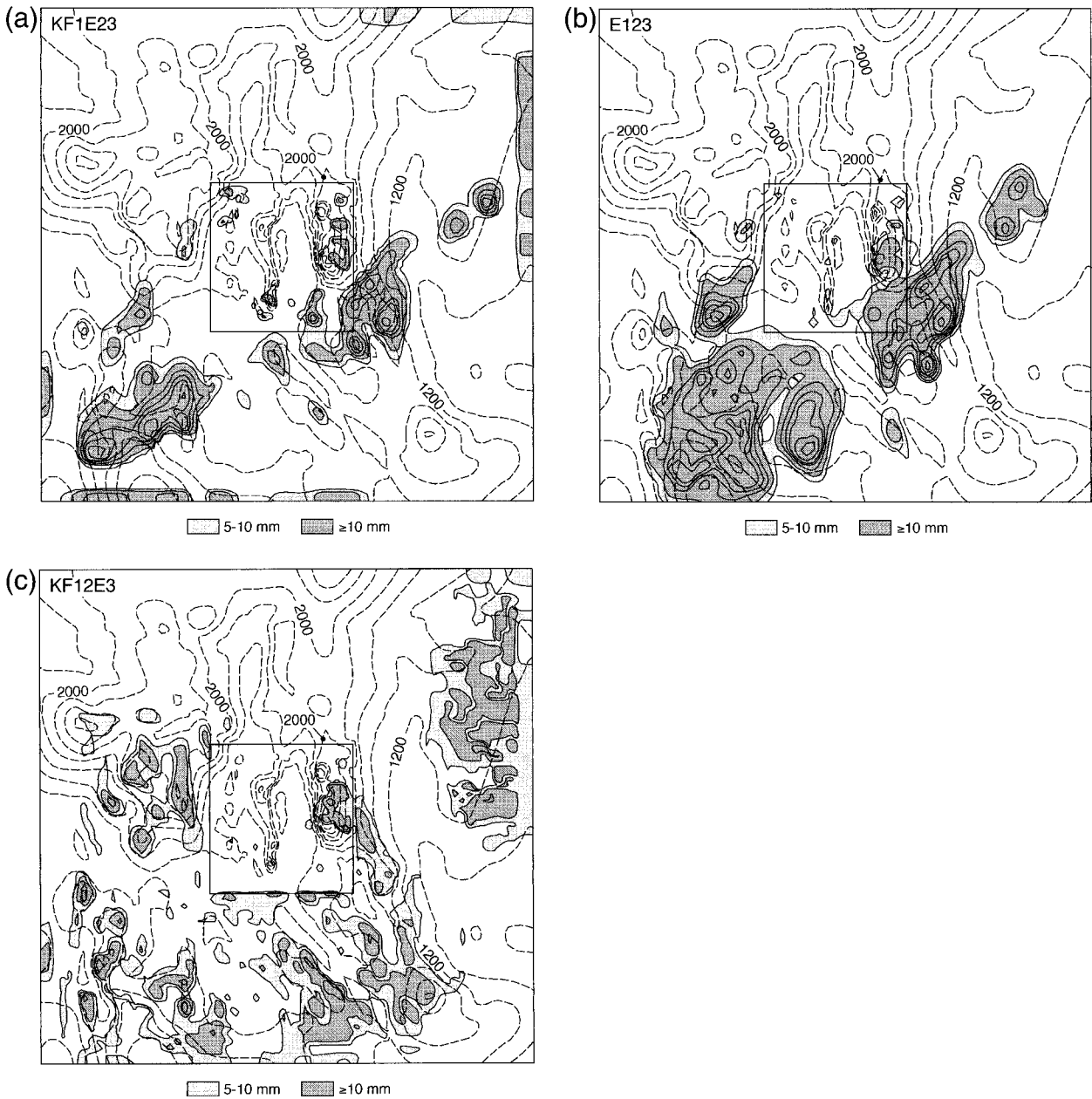


FIG. 13. Total simulated rainfall for the 24-h period from 1200 UTC 12 Aug to 1200 UTC 13 Aug 1997 for grids 2 and 3 for the designated experiments. Isohyets are plotted at irregular intervals with the following values (mm): 5, 10, 20, 30, and 40. Light shading reflects amounts of 5–10 mm, while darker shading is for values greater than 10 mm.

ing, while the shallower mode, which travels only half as fast, produces upward motion in the lower half of the layer and subsidence in the upper half. Because most heating profiles likely do not have simple vertical structure, the separation of the waves with distance will cause a complex response in the vertical motion. This is supported by Pandya and Durran (1996) who describe sensitivity studies that show that the characteristics of the mesoscale circulations around a squall line are more sensitive to the shape of the thermal forcing than to the properties of the convective environment through which

the gravity waves propagate. Bretherton estimates an *e*-folding distance of 12 000 km for turbulent dissipation in the stably stratified convective environment. The appropriate scale for rotation effects is the Rossby radius of deformation, where a typical midlatitude *e*-folding distance would be approximately 300–500 km for deep disturbances caused by a deep layer of latent heating. The vertical motion response is largely limited to this radius. The results of these modeling and theoretical studies are confirmed by observations. For example, Ni-nomiya (1971a,b) and others have documented that the

outflow area above thunderstorms can have dimensions of 500 km and produce dry areas around the storm. Johnson et al. (1995) describe how subsidence between two mesoscale convective systems along a cold front suppresses the development of convection in the several hundred kilometers between them. A similar situation was documented by Stensrud and Maddox (1988).

In order to document how outer grid CPs affect the grid 3 convective environment, a series of experiments was performed in which the grid 3 temperature, specific humidity, and vertical motion were compared with and without the CP effects from outer grids. No precipitation effects were permitted on grid 3, to allow a more straightforward interpretation of outer grid CP effects on the environment there. The three CPs were used on both of the outer two grids in experiments G12D3, BM12D3, and KF12D3 (see Table 1). The grid-3-average hourly vertical profiles of temperature, moisture, and vertical motion from these experiments were subtracted from the profiles from experiment D123 in which no moist effects were permitted on grids 1 and 2. The difference fields, or CP impact fields, isolate the effects of the different CPs on the grid 3 convective environment.

It should be noted that the temporal variations in these grid-3-average impact fields reflect the superposition of the CP effects from numerous areas of convection on both grids 1 and 2. In addition, it is worth keeping in mind a couple of points when relating the impact fields of vertical motion with those for temperature and moisture. First, the vertical motion is the field that corresponds directly to the effects on the grid 3 environment of the gravity waves initiated by the CPs, whereas the temperature and moisture impacts result from the temporally integrated effects of the vertical motions. Correlation of vertical motion with temperature is complicated by the fact that the temperature response of a layer to its vertical displacement is related to its static stability. In terms of the effects of vertical motion on moisture, lower-level vertical velocities will cause larger advective changes in the local moisture content because the gradients are larger.

Figure 14 shows time–height sections of the impact fields, with hourly resolution, for each of the three CPs. For all CPs, the CP impact is for enhanced weak (subsidence) warming early in the period throughout most of the troposphere, especially for the Betts–Miller CP, which has early heavy precipitation on grid 2. Very quickly, a vertical wavenumber 1 structure develops for all CPs, with warming above 600–700 hPa and cooling below. This evolution could be reflecting the rapid arrival on grid 3 of deep subsidence from fast, deep gravity modes, with the arrival later of higher vertical wavenumber slower modes with low-level upward motion and higher-level subsidence. The magnitude of the downward vertical gradient in these hourly temperature impact fields is proportional to the amount of stabilization of the grid 3 temperature lapse rate caused by

the outer grid CPs. Thus, the CPs generally caused an increase in static stability below about 600 hPa. The specific humidity impact fields show that the CPs cause drying on grid 3 below about 500 hPa, with limited areas of low-level moistening. The moistening (not the maximum) roughly correlates temporally and spatially with the low-level upward motion.

The Betts–Miller plots illustrate well the transition from the deep mode to a pattern with more vertical structure associated with a superposition of modes. In Fig. 9 it was shown that the Betts–Miller grid 2 precipitation develops rapidly during the first hour of the simulation, where some is located near the eastern grid 2–3 interface (not shown). A reasonable speed for the fast gravity mode is  $30 \text{ m s}^{-1}$ , and thus the associated subsidence could have traversed the entire area of grid 3 in less than 2 h. Therefore, the timing of the deep warming maximum at hour 3 in the Betts–Miller plot in Fig. 14 is reasonable. Again using this CP as an example, the appearance of the significant low-level cooling after hour 8 would correlate with the arrival on grid 3 of the slower modes having upward motion at low levels (see vertical motion panel in Fig. 14). Indeed, except for the early deep subsidence, the largest average vertical motion during the period is upward at low levels ( $\sim$ hour 11). It is generally straightforward to relate the changes in the sign of the vertical motion impact during the period to the sign of the temperature and humidity impacts, especially if one keeps in mind that vertical motion extrema correlate temporally with the *changes* in the temperature and moisture impact fields and not with their extrema.

Aside from the above broad similarities in the patterns, there are many distinctions associated with the different CPs. For example, the timing of the grid 2 precipitation, shown in Fig. 9, seems to correlate well with the timing of the onset of the grid 3 convective-environment modifications seen in Fig. 14. For the Betts–Miller CP, convection on grid 2 peaks during the first few hours, and the temperature and humidity changes to grid 3 first appear during this period, earlier than for any other CP. The Grell precipitation develops latest, and most realistically, on grid 2, and the higher-amplitude temperature and humidity effects on grid 3 appear later than for the other CPs. Also, there is a correlation between the magnitude of the convection suppression on grid 3, as implied by the grid 3 precipitation rates in Fig. 9, and the amplitude of the drying and static-stability increases on grid 3 seen in Fig. 14. For example, the grid 3 resolved precipitation is most strongly suppressed by the Kain–Fritsch parameterization on the outer grids (Fig. 8), and it is this parameterization that produces the greatest drying and the largest stabilization of lapse rates during the time when the precipitation should be developing on grid 3. Conversely, the most realistic precipitation on grid 3 is associated with the use of the Grell CP on the outer grids, and it is this CP that causes the least drying and smallest static stability

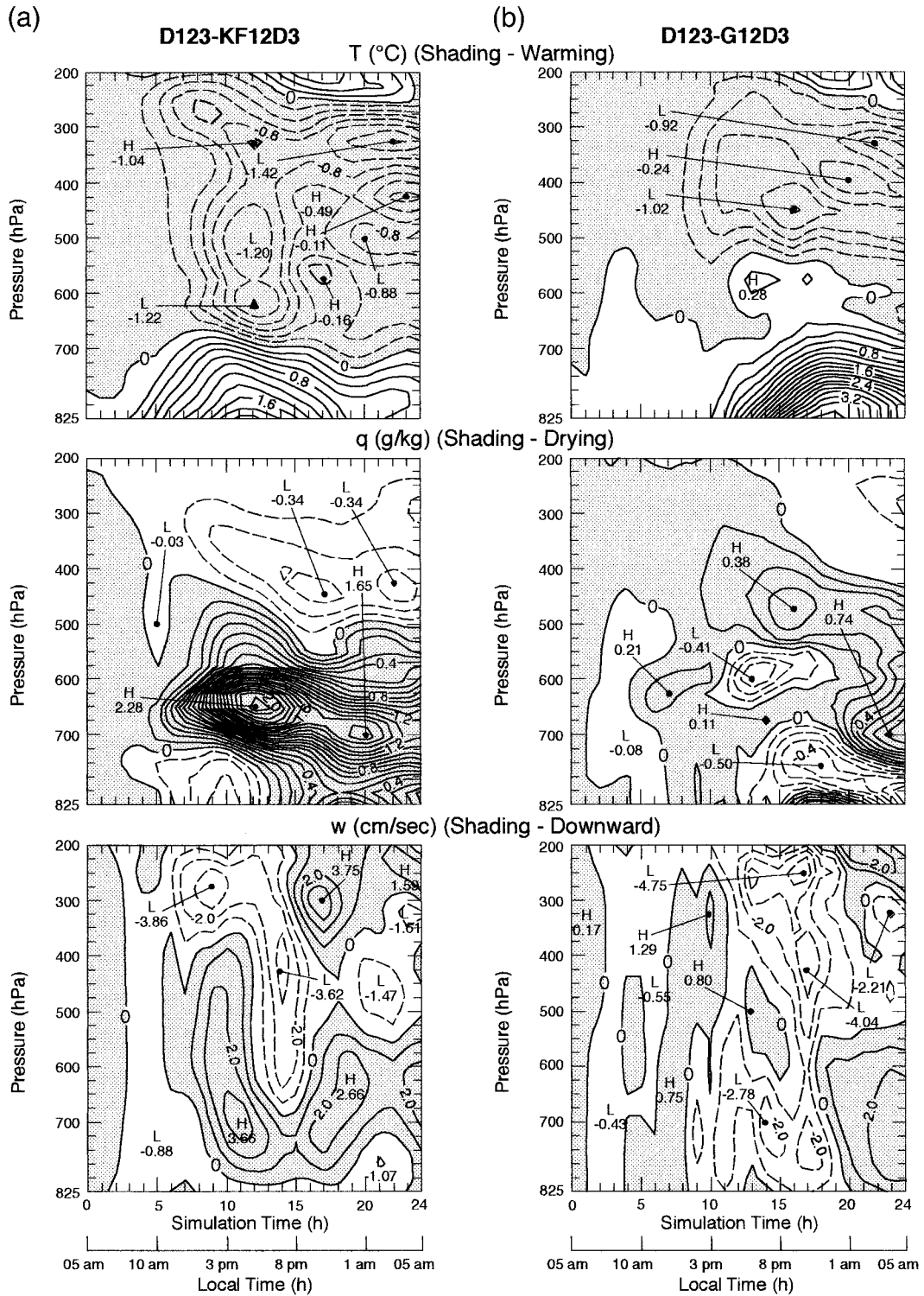


FIG. 14. Vertical time sections of grid-3-average temperature, specific humidity, and vertical velocity differences between experiments with CPs on grids 1 and 2 (G12D3, BM12D3, G12D3) and that with no moist processes on these grids (D123). No moist processes were permitted on grid 3. The difference fields show the effects of the outer grid CPs on the convective environment of grid 3.

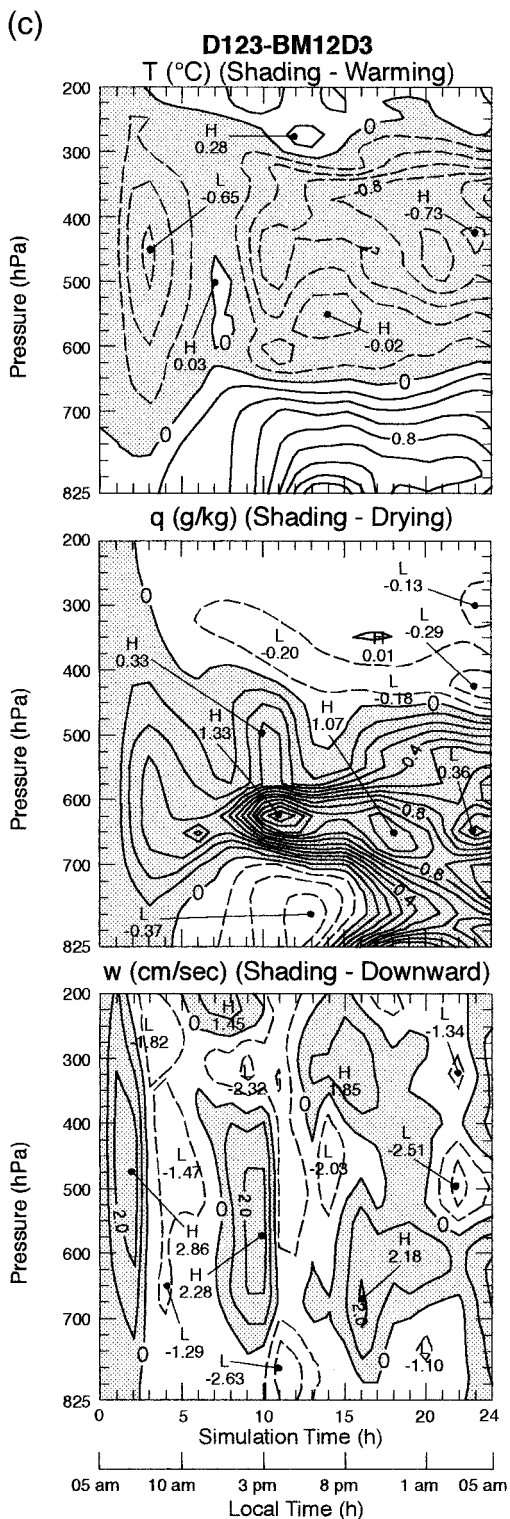


FIG. 14. (Continued)

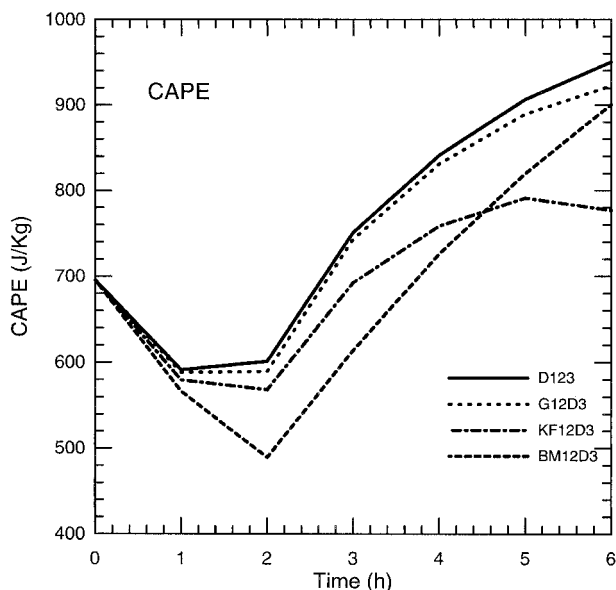
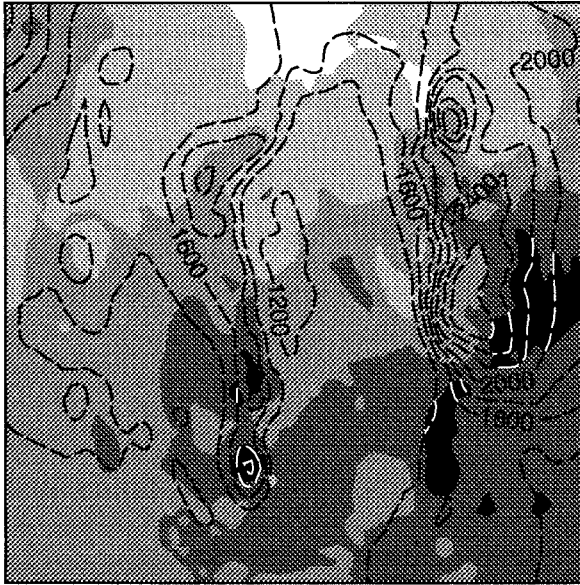


FIG. 15. Grid-3-average CAPE as a function of time for the first 6 h of the experiments indicated.

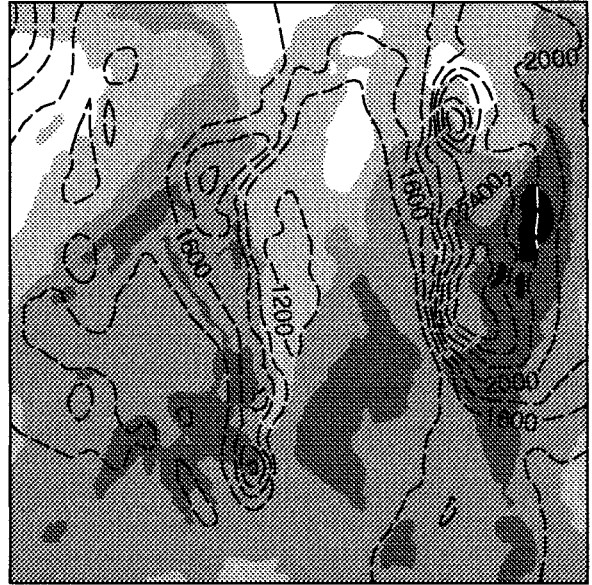
increases during the period of heaviest observed precipitation.

Useful metrics for summarizing the convective environment on grid 3 are the CAPE and the convective inhibition (CIN). The CAPE represents the work done on a parcel by the environment as it is accelerated upward from its level of free convection (LFC) to its equilibrium level. The CIN is the work required to lift a parcel from the surface to its LFC. The parcel properties are defined here as the mean in the lowest 500 m. Figure 15 shows the grid-3-average CAPE as a function of time for the first 6 h of experiments KF12D3, BM12D3, G12D3, and D123. These grid 3 CAPE plots begin to diverge soon after the grid 2 convection develops (Fig. 9). Divergence of the CAPE evolutions, of course, is entirely a result of the outer grid CPs. The grid 3 CAPE responds to outer grid precipitation first (after 1 h) in BM12D3 because the outer grid precipitation occurs first for that CP (Fig. 9). Subsequently, as KF12D3 begins to develop precipitation on grid 2, its grid 3 CAPE begins to diverge from that of experiment G12D3 for which grid 2 precipitation has not yet developed. Experiment D123, of course, has no outer grid moist effects to influence the grid 3 environment. Until about hour 5 when significant precipitation develops on grid 3 (Fig. 8), the grid 3 CAPE plots for these experiments are identical to the corresponding plots from the series of experiments that employs complete moist physics on grid 3 (e.g., KF12D3). After the time of precipitation initiation, CAPE is only consumed in the experiments with moist convection allowed on grid 3. Corresponding grid 3 CIN plots show differences among experiments, but they are not as significant. Figure 16 illustrates the horizontal variability in the effects of the outer grid CPs

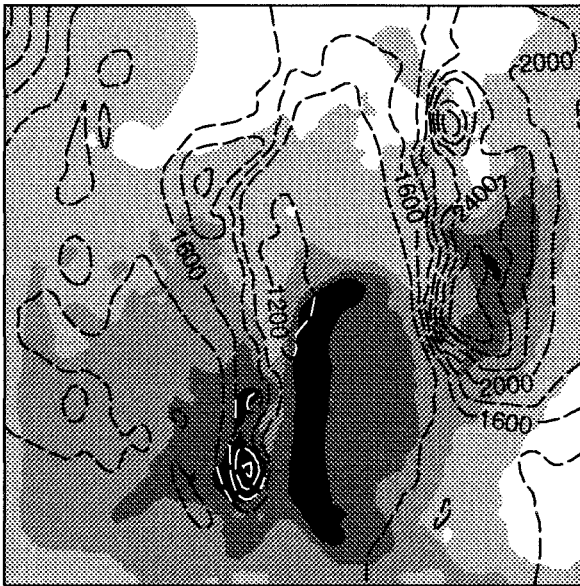
D123



BM12D3



G12D3



KF12D3

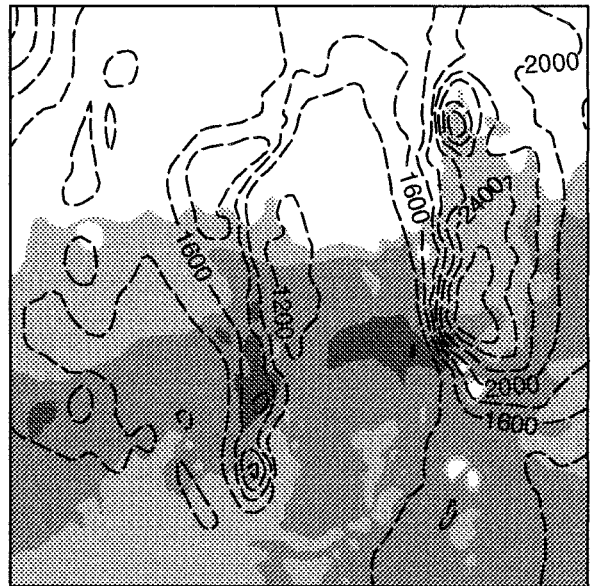


FIG. 16. Horizontal distribution of the grid 3 CAPE at hour 12 for the experiments indicated. The values of CAPE are plotted in  $J\ kg^{-1}$ . The dashed contours show terrain elevation labeled in m at an interval of 400 m.

on grid 3 CAPE at 12 h. Even though these values of CAPE are large because there are no grid 3 moist processes to consume the CAPE, the plots nevertheless serve as a good metric of the effects of the outer grid CPs on the inner grid convective environment.

To complement the discussion of the grid-3-average effects just described, Fig. 17 shows an example of the evolution of specific temperature and dewpoint temperature profiles on grid 3. The grid point that is closest to the southern terrain elevation maximum of the Sac-

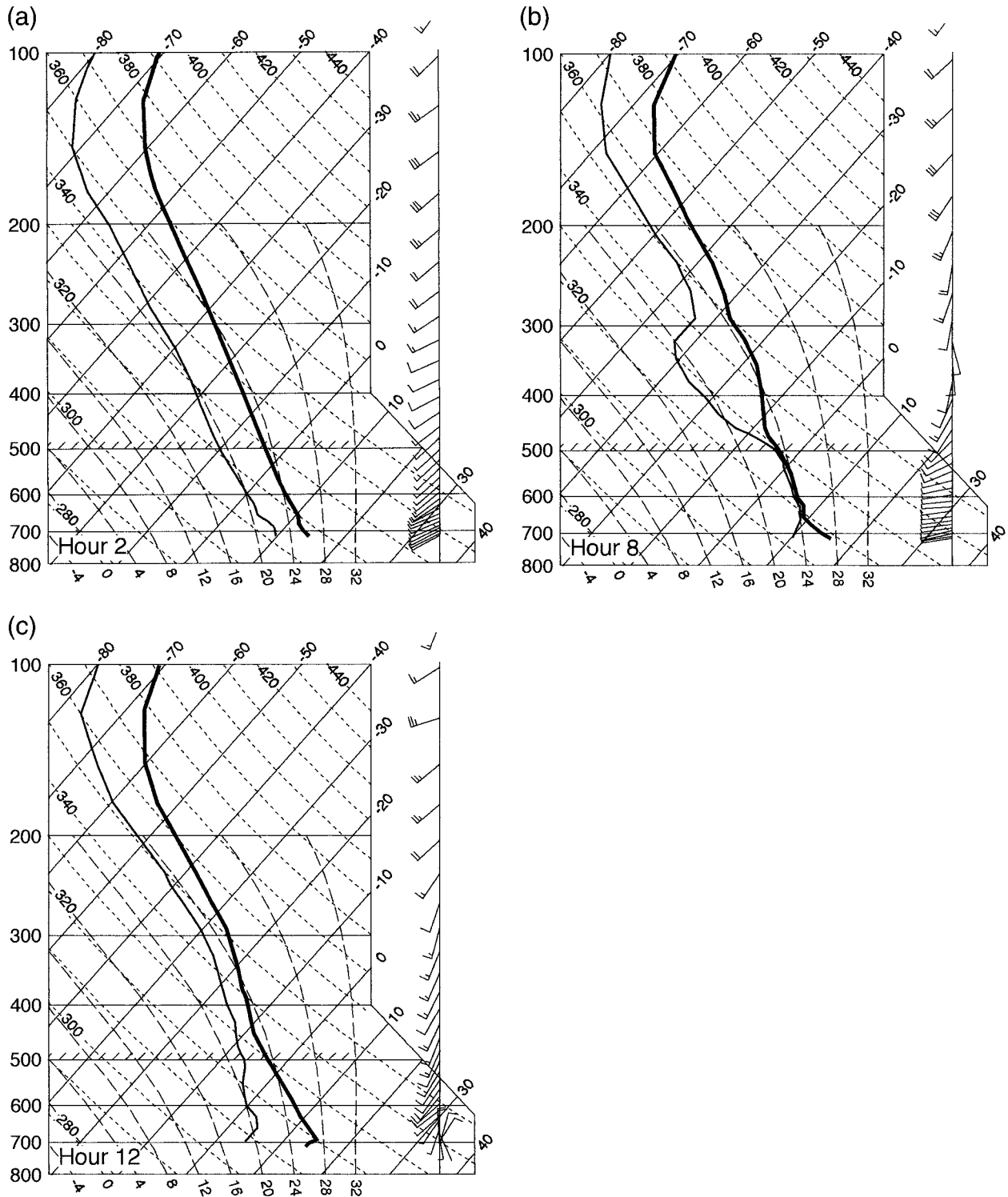


FIG. 17. Vertical profiles of temperature and dewpoint temperature at simulation hours 2, 8, and 12 for the model grid point nearest the southernmost elevation maximum in the Sacramento Mountains in grid 3 of experiment KF12E3 (see “×” symbol in Fig. 1).

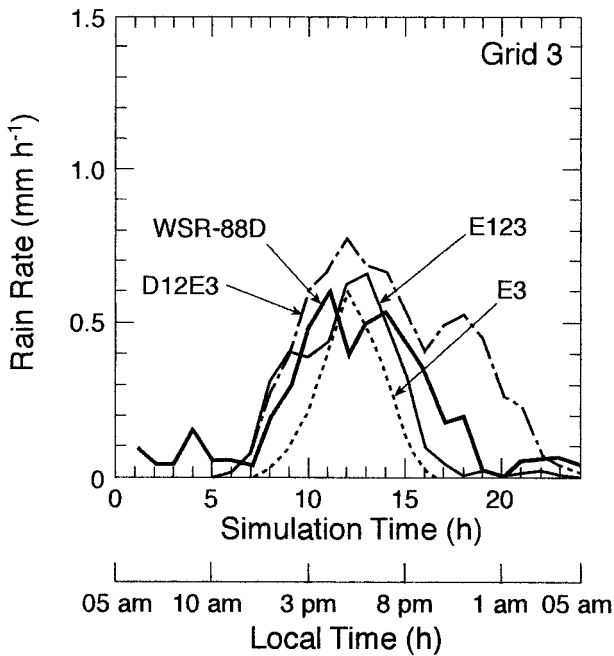


FIG. 18. Grid-3-average rain rate ( $\text{mm h}^{-1}$ ) as a function of time during the 24-h simulation from 1200 UTC (0500 LST) 12 Aug to 1200 UTC 13 Aug 1997. Plots are shown for experiments D12E3, E123, and E3, and for the observed precipitation as estimated from the Holoman WSR-88D radar.

ramento Mountains (see “x” marked in Fig. 1c) was chosen. Experiment KF12E3 will be utilized as an example because the cessation of simulated rainfall was most premature for that experiment (Fig. 8). Figure 17 shows the profiles at simulation hours 2, 8, and 12. This particular temperature sounding does not change significantly, remaining approximately moist adiabatic during the period. However, the dewpoint temperature increases until saturation is reached by hour 5, the depth of the saturated layer reaches a maximum by hour 8, and by hour 11 the atmosphere below 500 hPa has dried dramatically so that the entire column is subsaturated. Relative to this point, the nearest separate area of substantial convection is over 150 km away on grid 2.

In order to help further isolate the effects of the outer grid CPs on the resolved convection, two additional experiments (E3 and D12E3) were performed. In experiment E3, no outer grids were used, and the LBCs for the convection-resolving grid were defined based on NCEP analyses. Thus, only large-scale information was provided to grid 3. To provide a more controlled experiment in which CP effects are not permitted to influence grid 3 convection, but where other coarse-grid processes are, experiment D12E3 was performed in which all precipitation effects were eliminated from grids 1 and 2.

Figure 18 shows that the temporal distribution of the precipitation in E3 is similar to that from E123, even though the initiation time is late. The spatial distribution

of the rainfall (not shown) is qualitatively similar to the patterns from the other experiments, with most of the accumulation being over the Sacramento Mountains. In some respects it can be argued that this simulation that is produced *without* the use of a nested grid system is superior to *some of* the simulations that employ the nest, such as KF12E3. It should be pointed out that the removal of the outer two grids in this experiment has more impact on grid 3 than simply through the elimination of the effects of the CPs. That is, in E3 there is *no* mesoscale signal of any kind in the LBC information. For experiment D12E3, except for the erroneous simulated nocturnal rainfall, it is a reasonable claim that this simulation of rainfall amount and temporal distribution is as good as or better than that of all the other experiments, with a realistic initiation time and rain rate. In fact, it did better than all the other experiments in reproducing (not shown) the northeast–southwest-oriented band of 24-h total rainfall in the southern Tularosa Valley (Fig. 4). This is an ironic situation because the implication is that these CPs on the outer grids have more of a negative than a positive impact on the resolved convection on the inner grid.

## 5. Summary and discussion

The results of the above-described experiments are summarized below.

- The different CPs employed produce considerably different simulations of rainfall, even though these differences are not uncharacteristically large relative to CP comparisons in other studies (Wang and Seaman 1997).
- The characteristics of the convective parameterizations on the coarse grids have a large impact on the resolved rainfall on the convection-resolving grid.
- The timescale with which the parameterized rainfall on the coarse grids affects the resolved-scale precipitation is very short (less than 1 h).
- Even when the use of a CP is limited to the outermost grid of the three, there are significant CP impacts on the resolved convective rainfall on the inner grid. The timescale for this response is also rapid, even though the effect of the differences in the CPs on the outer grid has to pass through the intermediate-resolution grid before impacting the convection-resolving grid.
- For the intermediate-resolution grid 2 ( $\Delta x = 10$  km), more accurate rainfall is generally obtained from simulations that did not employ a CP on that grid. The better rain rates on this grid are associated with better rainfall simulations on the inner grid.
- On the convection-resolving grid, the timing of the initiation and decay of the convection is generally simulated well, regardless of the CPs employed on the outer grids. However the total amount of rainfall and the timing of the peak rain rate are generally not simulated well, often because the simulated rainfall

- seems to be suppressed after experiencing normal development for the first few hours of the diurnal cycle.
- Comparison of grid-3-averaged temperature, humidity, and vertical motion distribution with and without the use of CPs on grids 1 and 2 demonstrates the existence of major differences in the grid 3 impacts of the CPs. The general consequences of the CP-induced vertical motion are 1) warming above 600–700 hPa and cooling below, and 2) drying between 500 and 700 hPa, with some moistening below. The strongest induced stabilization and drying is produced by the Kain–Fritsch and Betts–Miller CPs, that also produce the greatest suppression of precipitation on grid 3. The timing of the maxima in the CP-induced stabilization and drying correspond with the periods during the observed precipitation when the simulated precipitation is deficient.
  - When rainfall simulations on the convection-resolving grid are insulated from coarse-grid parameterized convective effects through the drastic measures of eliminating coarse-grid moist physics or eliminating the entire coarse grids, the quality of the simulation of the resolved convection is improved compared to that from at least some of the simulations with parameterized moist physics on the coarser meshes.

The most intriguing questions are 1) what is the mechanism by which the parameterized convection influences the resolved convection on such short timescales and over considerable distances and 2) why is the impact so large, on the resolved-scale convection, of these fairly typical differences in rainfall simulated by the different CPs.

In answer to the first question, the rapidity of the response of the rainfall on the convection-resolving grid to distant differences in the parameterized convection on the surrounding grids implies that 1) advective or outflow-boundary effects cannot be responsible and 2) convection-related mass field adjustments across the nested computational grids are the likely mechanism that links the resolved convection on the fine grid with the parameterized convection of the coarser grids. That is, parameterized convection with a time evolution and spatial distribution that is inconsistent with the explicitly resolved convection produces mass-field adjustments that incorrectly affect the convective environment on the convection-resolving grid. In this case, a drying and stabilization of the model soundings after convection is initiated on the convection-resolving grid(s) is responsible for the premature shutdown of convection after a normal development for the first few hours of the diurnal cycle. These effects seem to result from erroneous mass-field adjustments to the parameterized convection on the coarser grids.

Regarding the second question, in the atmosphere there is a natural interaction among different areas of convection. The nature of the interaction, which depends on the proximity of the convective areas, includes com-

petition for boundary layer moisture and modification of the environment through induced vertical motion. An interesting question is whether this natural competition among convective areas in the atmosphere is simulated well in a nested model where convection is parameterized on one grid and explicitly resolved on another. For example, consider equivalent areas of convection that develop approximately simultaneously on two such grids within a nested system; is there a normal, that is, physically realistic, competition between the convective areas, or does one dominate for purely numerical reasons? This question is obviously important in the context of the present study. The qualitative answer is that there definitely is an inherent and unavoidable nonphysical aspect to the competition between parameterized and explicit convection. For example, the parameterized convection, depending on the cloud model employed, may not be as sensitive to subsidence-related drying or stabilization in the environment as is the explicit convection. Or, even though the explicit and parameterized convection may initiate simultaneously, and the parameterized convection may develop the correct rain rates, the parameterized convection may develop too rapidly after initiation and suppress the explicit convection early in its life cycle. The possible mechanisms for nonphysically realistic competition between areas of resolved and parameterized convection are numerous, and depend on the specific parameterization employed. However, even with *perfect* CPs, the competition between resolved and parameterized convection is inherently nonphysical. This is related to the fact that the gravity waves created by the latent heating on the convection-resolving grid contain higher wavenumber components than those created by the coarser latent-heating field on the outer (coarser) grids with parameterized convection. The higher wavenumber components originating on the fine grid are going to be adversely affected (partially reflected, aliased, damped) as they pass outward to a coarser grid through even a well-designed nest interface. However, the longer gravity waves generated by the CPs crossing the interface in the other direction will not be adversely affected in the same ways. Further work is required to determine how this problem affects the resolved convection.

The conclusions described here are obviously based on only one case. Case-dependent aspects of the results likely include

- the relative skill of the different CPs,
- the nature of the resolved convection in terms of how strongly it is forced by local conditions or mesoscale dynamics,
- the horizontal resolution required to successfully simulate convective processes explicitly, and
- the relative skill with which convection is simulated with and without parameterizations at intermediate model resolutions (e.g.,  $\Delta x = 10$  km).

However, it is felt that the demonstrated sensitivity of

the resolved convection to the parameterized convection on surrounding grids in a nested system is sufficiently robust that it is not a peculiarity of the case chosen for study.

Clearly, the results described here have considerable implications for high-resolution operational numerical prediction of convective weather using nested modeling systems. In this study, the emphasis has been on the identification and documentation of one of the challenges that must be addressed, that is, the sensitivity of the resolved convection to the surrounding parameterized convection. The province of future work will be to investigate modeling techniques that will minimize the problems identified here. It is intuitive that possible measures for mitigating the problem may include the following:

- utilizing sufficiently large convection-resolving grids so that coarse-grid effects will not penetrate, even on gravity–inertia wavetime scales, to the area of convection during the duration of the simulation (the computational cost of this would be prohibitive, except in a research setting);
- utilization of CPs that produce physically reasonable local mass-field responses to the convection, such that the interaction with other areas of convection is realistic;
- identifying CPs that can be tuned such that there is minimal nonphysical competition between explicitly resolved and parameterized convection; and
- continuing to test the adequacy of marginal grid resolutions ( $\Delta x = 3\text{--}5$  km) for the explicit simulation of convection.

*Acknowledgments.* This research was funded by the U.S. Army Test and Evaluation Command through an Interagency Agreement with the National Science Foundation. Additional support was through special funds from the National Science Foundation that have been designated for the U.S. Weather Research Program activities at NCAR. The authors gratefully acknowledge useful discussions with, and suggestions by, Jack S. Kain, Morris L. Weisman, Brian E. Mapes, and J. Michael Fritsch.

#### REFERENCES

- Betts, A. K., and M. J. Miller, 1993: The Betts–Miller scheme. *The Representation of Cumulus Convection in Numerical Models, Meteor. Monogr.*, No. 46, Amer. Meteor. Soc., 107–121.
- Black, T., M. Baldwin, G. DiMego, and E. Rogers, 1998: Results from daily forecasts of the NCEP Eta-10 model over the western United States. Preprints, *12th Conf. on Numerical Weather Prediction*, Phoenix, AZ, Amer. Meteor. Soc., 246–247.
- Bretherton, C. S., 1987: A theory for nonprecipitating moist convection between two parallel plates. Part I: Thermodynamic and “linear” solutions. *J. Atmos. Sci.*, **44**, 1809–1827.
- , and P. K. Smolarkiewicz, 1989: Gravity waves, compensating subsidence and detrainment around cumulus clouds. *J. Atmos. Sci.*, **46**, 740–759.
- Carpenter, R. L., Jr., and Coauthors, 1998: Storm-scale NWP for commercial aviation: Results from real-time operational tests in 1996–1997. Preprints, *12th Conf. on Numerical Weather Prediction*, Phoenix, AZ, Amer. Meteor. Soc., 213–216.
- Cram, J. M., R. A. Pielke, and W. R. Cotton, 1992: Numerical simulation and analysis of a prefrontal squall line. Part II: Propagation of the squall line as an internal gravity wave. *J. Atmos. Sci.*, **49**, 209–225.
- Davis, C., H.-M. Hsu, T. Keller, A. Shantz, and T. Warner, 1998: A meso- $\gamma$ -scale real time forecasting system suitable for regions of complex terrain. Preprints, *12th Conf. on Numerical Weather Prediction*, Phoenix, AZ, Amer. Meteor. Soc., 223–225.
- Dudhia, J., 1989: Numerical study of convection observed during the winter monsoon experiment using a mesoscale two-dimensional model. *J. Atmos. Sci.*, **46**, 3077–3107.
- , 1993: A nonhydrostatic version of the Penn State/NCAR mesoscale model: Validation tests and the simulation of an Atlantic cyclone and cold front. *Mon. Wea. Rev.*, **121**, 1493–1513.
- Grell, G. A., 1993: Prognostic evaluation of assumptions used by cumulus parameterizations. *Mon. Wea. Rev.*, **121**, 764–787.
- , J. Dudhia, and D. R. Stauffer, 1994: A description of the fifth generation Penn State/NCAR Mesoscale Model (MM5). NCAR Tech. Note NCAR/TN 398+STR, 138 pp.
- Hong, S.-Y., and H.-L. Pan, 1996: Nonlocal boundary layer vertical diffusion in a medium-range forecast model. *Mon. Wea. Rev.*, **124**, 2322–2339.
- Janjic, Z. I., 1994: The step-mountain eta coordinate model: Further developments of the convection, viscous sublayer, and turbulence closure schemes. *Mon. Wea. Rev.*, **122**, 927–945.
- Johnson, R. H., B. D. Miner, and P. E. Ciesielski, 1995: Circulations between mesoscale convective systems along a cold front. *Mon. Wea. Rev.*, **123**, 585–599.
- Kain, J. S., and J. M. Fritsch, 1990: A one-dimensional entraining/detraining plume model and its application in convective parameterization. *J. Atmos. Sci.*, **47**, 2784–2802.
- , and —, 1993: Convective parameterization for mesoscale models: The Kain–Fritsch scheme. *The Representation of Cumulus Convection in Numerical Models, Meteor. Monogr.*, No. 46, Amer. Meteor. Soc., 165–170.
- Mapes, B. E., 1993: Gregarious tropical convection. *J. Atmos. Sci.*, **50**, 2026–2037.
- Molinari, J., and M. Dudek, 1992: Parameterization of convective precipitation in mesoscale numerical models: A critical review. *Mon. Wea. Rev.*, **120**, 326–344.
- Nicholls, M. E., R. A. Pielke, and W. R. Cotton, 1991: Thermally forced gravity waves in an atmosphere at rest. *J. Atmos. Sci.*, **48**, 1869–1884.
- Ninomiya, K., 1971a: Dynamical analysis of outflow from tornado-producing thunderstorms as revealed by ATS III pictures. *J. Appl. Meteor.*, **10**, 275–294.
- , 1971b: Mesoscale modifications of synoptic situations from thunderstorm development as revealed by ATS III and aerological data. *J. Appl. Meteor.*, **10**, 1103–1121.
- Pandya, R. E., and D. R. Durran, 1996: The influence of convectively generated thermal forcing on the mesoscale circulation around squall lines. *J. Atmos. Sci.*, **53**, 2924–2951.
- Schultz, P., 1998: Status and prospects for local data analysis and mesoscale modeling in AWIPS. Preprints, *12th Conf. on Numerical Weather Prediction*, Phoenix, AZ, Amer. Meteor. Soc., 324.
- Seaman, N. L., S. A. Michelson, P. C. Shafran, and D. R. Stauffer, 1998: Forecast of a severe squall line development in MM5 using explicit moist physics at 4-km resolution. Preprints, *12th Conf. on Numerical Weather Prediction*, Phoenix, AZ, Amer. Meteor. Soc., J1–J4.
- Snook, J. S., P. A. Stamus, J. Edwards, Z. Christidis, and J. A. McGinley, 1998: Local-domain mesoscale analysis and forecast model support for the 1996 Centennial Olympic Games. *Wea. Forecasting*, **13**, 138–150.
- Stensrud, D. J., and R. A. Maddox, 1988: Opposing mesoscale circulations: A case study. *Wea. Forecasting*, **3**, 189–204.
- Szoke, E. J., J. A. McGinley, P. Schultz, and J. S. Snook, 1998: Near-

- operational short-term forecasts from two mesoscale models. Preprints, *12th Conf. on Numerical Weather Prediction*, Phoenix, AZ, Amer. Meteor. Soc., 320–323.
- Troen, I., and L. Mahrt, 1986: A simple model of the atmospheric boundary layer: Sensitivity to surface evaporation. *Bound.-Layer Meteor.*, **37**, 129–148.
- Wang, W., and N. L. Seaman, 1997: A comparison study of convective parameterization schemes in a mesoscale model. *Mon. Wea. Rev.*, **125**, 252–278.
- Warner, T. T., Y.-H. Kuo, J. D. Doyle, J. Dudhia, D. R. Stauffer, and N. L. Seaman, 1992: Nonhydrostatic, mesobeta-scale real-data simulations with the Penn State University/National Center for Atmospheric Research mesoscale model. *Meteor. Atmos. Phys.*, **49**, 209–227.
- , R. A. Petersen, and R. E. Treadon, 1997: A tutorial on lateral boundary conditions as a basic and potentially serious limitation to regional numerical weather prediction. *Bull. Amer. Meteor. Soc.*, **78**, 2599–2617.
- Weisman, M. L., W. C. Skamarock, and J. B. Klemp, 1997: The resolution dependence of explicitly modeled convective systems. *Mon. Wea. Rev.*, **125**, 527–548.